

A refined search for high-velocity gas in the Cygnus Loop supernova remnant

Adam M. Ritchey,^{1*} S. R. Federman,² and David L. Lambert³

¹*Eureka Scientific, 2452 Delmer, Suite 100, Oakland, CA 96402, USA*

²*Department of Physics and Astronomy, University of Toledo, Toledo, OH 43606, USA*

³*W. J. McDonald Observatory and Department of Astronomy, University of Texas at Austin, Austin, TX 78712, USA*

Accepted XXX. Received YYY; in original form ZZZ

ABSTRACT

We present the results of a sensitive search for high-velocity gas in interstellar absorption lines associated with the Cygnus Loop supernova remnant (SNR). We examine high-resolution, high signal-to-noise ratio optical spectra of six stars in the Cygnus Loop region with distances greater than ~ 700 pc. All stars show low-velocity Na I and Ca II absorption. However, only one star, HD 198301, exhibits high-velocity Ca II absorption components, at velocities of +62, +82, and +96 km s⁻¹. The distance to this star of ~ 870 pc helps to constrain the distance to the receding edge of the Cygnus Loop’s expanding shock front. One of our targets, HD 335334, was previously thought to exhibit high positive and high negative velocity interstellar Na I and Ca II absorption. This was one factor leading Fesen et al. to derive a distance to the Cygnus Loop of 725 ± 15 pc. However, we find that HD 335334 is in fact a double-line spectroscopic binary and shows no evidence of high-velocity interstellar absorption. As such, the distance to HD 335334 cannot be used to constrain the distance to the Cygnus Loop. Our detection of Ca II absorption approaching 100 km s⁻¹ toward HD 198301 is the first conclusive detection of high-velocity absorption from a low ionization species associated with the Cygnus Loop SNR. A large jump in the Na I column density toward BD+31 4218, a star located beyond the northwestern boundary of the Cygnus Loop, helps to constrain the distance to a large molecular cloud complex with which the Cygnus Loop is evidently interacting.

Key words: ISM: individual objects; Cygnus Loop – ISM: abundances – ISM: kinematics and dynamics – ISM: supernova remnants

1 INTRODUCTION

The Cygnus Loop supernova remnant (SNR), also known as the Veil Nebula, is one of the best-studied evolved Galactic SNRs owing to its relative brightness, its large angular size, and the absence of a significant amount of foreground extinction along the line of sight. With an extensive network of well-resolved filamentary structures, the Cygnus Loop SNR is an excellent laboratory for investigations into various shock-related phenomena, including cloud-shock interactions (e.g., Danforth et al. 2001; Patnaude et al. 2002), X-ray, UV, and optical emission from pre- and post-shock gas (e.g., Sankrit et al. 2000; Blair et al. 2002; Salvesen et al. 2009; Medina et al. 2014; Raymond et al. 2023), and dust grain destruction via shock sputtering (e.g., Sankrit et al. 2010; Raymond et al. 2013).

However, despite its relative proximity, an accurate distance to the Cygnus Loop SNR has been difficult to determine. Minkowski (1958) derived a distance of 770 pc from a kinematic investigation of the remnant’s bright optical filaments. More recent distance estimates, mainly from proper motion studies, show considerable variation, ranging from 440 pc to 1400 pc (see the summary of results provided by Fesen et al. 2018a). As with any SNR, the distance to the Cygnus Loop is a key parameter for understanding many fundamental prop-

erties of the remnant, including the shock speed, the gas pressure, and the SN explosion energy.

Blair et al. (2009) detected high-velocity interstellar O VI absorption toward the subdwarf OB star KPD 2055+3111, which is positioned among the bright optical filaments in the eastern portion of the Cygnus Loop (known as the Eastern Veil Nebula). From an analysis of the star’s optical spectrum, Blair et al. (2009) obtained stellar parameters that allowed them to calculate a distance of 576 ± 61 pc to KPD 2055+3111. Since this star presumably lies behind the Cygnus Loop SNR, its distance sets a hard upper limit on the distance to the Cygnus Loop. However, Gaia EDR3 parallax measurements indicate that the distance to KPD 2055+3111 is 819^{+21}_{-18} pc (Bailer-Jones et al. 2021), significantly larger than the estimate by Blair et al. (2009).

Fesen et al. (2018a) estimated the distance to the Cygnus Loop based on the distances to two stars they suggested are interacting with the remnant. One of the stars, a red giant with the designation TYC 2688-1037-1, is surrounded by a faint emission nebula, which Fesen et al. (2018a) proposed may be due to the interaction between the SNR blast wave and mass-loss material from the star. However, the Gaia EDR3 distance to TYC 2688-1037-1 is 2160 ± 130 pc (Bailer-Jones et al. 2021), indicating that this star is located far behind the Cygnus Loop SNR. Fesen et al. (2018a) also observed a bow-shaped nebula near the star BD+31 4224, and suggested that a bow shock was created by the interaction between the star’s stellar

* E-mail: ritchey.astro@gmail.com

wind and the remnant’s expanding shock front. The Gaia EDR3 distance to BD+31 4224 is 726_{-11}^{+13} pc (Bailer-Jones et al. 2021). Thus, a connection with the Cygnus Loop SNR is plausible.

In a subsequent study, Fesen et al. (2018b) searched for high-velocity interstellar Na I and Ca II absorption toward several stars in the Cygnus Loop region. Fesen et al. (2018b) claimed to discover high velocity gas toward three stars: HD 335334, TYC 2688-365-1, and TYC 2692-3378-1. Based on their discovery of high velocity gas, and adopting Gaia DR2 distances to the stars, Fesen et al. (2018b) constrained the distance to the Cygnus Loop SNR to be 735 ± 25 pc. More recently, Fesen et al. (2021) revised their distance estimate to 725 ± 15 pc, based on Gaia EDR3 measurements of the stars previously found to exhibit high-velocity interstellar absorption.

There is a problem with the conclusions of Fesen et al. (2018b), however. These authors used low resolution spectra (with $\Delta v \approx 30\text{--}45$ km s⁻¹) to search for high-velocity interstellar Na I and Ca II absorption lines. As we will show in this work, the star with the clearest signature of high-velocity absorption, HD 335334, is actually a double-line spectroscopic binary. The “high-velocity” components observed by Fesen et al. (2018b) toward this star are actually the stellar Na I D and Ca II K lines from the primary and the secondary. After accounting for stellar absorption, there are no high-velocity interstellar Na I or Ca II components toward HD 335334. The distance to this star, therefore, cannot be used to constrain the distance to the Cygnus Loop. The other two stars that Fesen et al. (2018b) claimed show high-velocity gas exhibit narrow low-velocity interstellar Na I components superimposed onto what appear to be broad stellar Na I absorption lines. (The Ca II K line in the spectrum of TYC 2692-3378-1 also appears to be very broad.) Thus, the “high-velocity” components in these cases are likely just the wings of the broad stellar absorption features.

A previous attempt by Welsh et al. (2002) to search for high-velocity interstellar Na I and Ca II absorption toward stars in the vicinity of the Cygnus Loop failed to detect any absorption features with velocities greater than ~ 30 km s⁻¹ (relative to the local standard of rest; LSR). In hindsight, this failure may, at least in part, be due to the fact that most of the stars observed by Welsh et al. (2002) have Gaia EDR3 distances of less than ~ 630 pc, and so may lie in front of the SNR. Moreover, the most distant star observed by Welsh et al. (2002), HD 197702, lies significantly outside the boundary of the remnant, as deduced from the bright H α emission contours (see, e.g., Figure 1 in Welsh et al. 2002), and so would not be expected to show high-velocity interstellar gas.

In this investigation, we present a new sensitive search for high-velocity interstellar absorption associated with the Cygnus Loop SNR. We examine high-resolution ($\Delta v \approx 4.5$ km s⁻¹), high signal-to-noise (S/N) ratio optical spectra of six stars in the Cygnus Loop region with Gaia EDR3 distances of ~ 700 pc or greater. We detect high-velocity Ca II absorption components (with LSR velocities approaching 100 km s⁻¹) toward only one star: HD 198301. This is the first conclusive detection of high-velocity Ca II absorption associated with the Cygnus Loop. Our observations and data reduction procedures are described in Section 2. In Section 3.1, we explain how we carefully separated stellar absorption lines from interstellar absorption features for our targets. In Section 3.2, we describe the profile fitting routine used to obtain interstellar column densities and component structures. We compare our survey with that of Welsh et al. (2002) in Section 3.3. The implications of our results for distance estimates to the Cygnus Loop SNR are discussed in Section 4. Our main conclusions are presented in Section 5. In Appendix A, we give a brief explanation of the procedures used to derive spectral types and luminosity classes for our program stars. (Prior to our study, most of

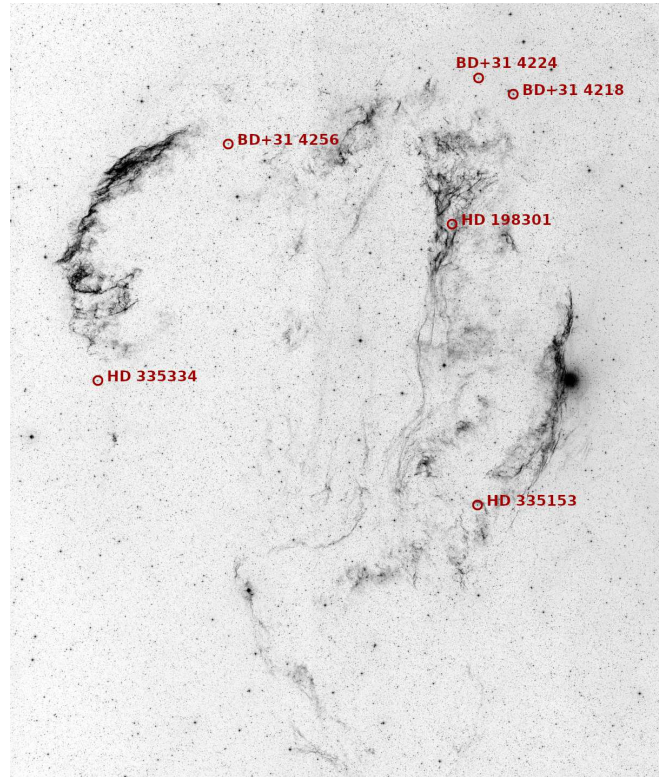


Figure 1. Optical image of the Cygnus Loop supernova remnant from the Digitized Sky Survey (DSS2 red). The six stars targeted for our observing program are indicated.

our targets had only limited information available concerning their spectral classification.)

2 OBSERVATIONS AND DATA REDUCTION

Six stars were observed using the Tull spectrograph (TS23; Tull et al. 1995) on the 2.7 m Harlan J. Smith Telescope at McDonald Observatory over the course of six nights in 2022 September. The targets were selected based on several criteria. Each potential target was required to have a Gaia EDR3 distance of 700 pc or greater and to be positioned within or very near the optical boundary of the Cygnus Loop SNR. We then selected stars with B and V magnitudes less than 10 so that high S/N ratio optical spectra could be acquired within a reasonable amount of time. The on-sky positions of the six targets in relation to the optical nebulosities associated with the Cygnus Loop are shown in Figure 1. Note that our target list includes BD+31 4224, which Fesen et al. (2018a) suggested is interacting with the Cygnus Loop, and HD 335334, which Fesen et al. (2018b) claimed shows high-velocity interstellar absorption. We had planned on obtaining data for a seventh target, HD 335249. However, due to adverse weather conditions at the beginning of the run, we decided to eliminate this relatively faint star from the target list.

Basic information regarding the target stars is provided in Table 1. The coordinates and B and V magnitudes are from the SIMBAD database (Wenger et al. 2000). The spectral types listed were derived in this work (see Appendix A). The values of $E(B-V)$ were determined based on the derived spectral types, using intrinsic colors from Wegner (1994). The distances provided in Table 1 are those derived from Gaia EDR3 parallax measurements (Bailer-Jones et al. 2021).

Table 1. Stellar and observational data for the program stars. The spectral types listed are those derived in this work (see Appendix A). Stellar coordinates and B and V magnitudes are from the SIMBAD database (Wenger et al. 2000). Values of $E(B-V)$ were determined using intrinsic colors from Wegner (1994). The distances provided are from Gaia EDR3 parallax measurements (Bailer-Jones et al. 2021). The last column gives the total exposure time on each target.

Star	Sp. Type	R. A. (J2000)	Dec. (J2000)	B (mag)	V (mag)	$E(B-V)$ (mag)	d (pc)	Exp. Time (s)
BD+31 4218	B2 IVe	20 47 01.93	+32 09 26.6	8.93	8.80	0.33	1121^{+22}_{-19}	7200
HD 335153	B9 III-IV	20 47 49.67	+30 05 31.0	9.56	9.56	0.07	700^{+11}_{-11}	10800
BD+31 4224	B7 V	20 47 51.82	+32 14 11.4	9.53	9.58	0.08	726^{+13}_{-11}	10800
HD 198301	B8 IV	20 48 28.26	+31 30 11.2	8.62	8.66	0.06	872^{+21}_{-11}	16200
BD+31 4256	B9 III-IV	20 53 47.40	+31 53 28.4	9.23	9.24	0.06	948^{+17}_{-20}	9000
HD 335334	B9 V	20 56 44.63	+30 41 14.4	9.54	9.51	0.10	732^{+12}_{-11}	14400

The TS23 configuration of the Tull spectrograph, when combined with a 2048×2048 CCD, provides nearly complete wavelength coverage of the optical spectrum, from ~ 3700 – $10,100 \text{ \AA}$, at a nominal resolving power of $R = 60,000$. Exposure times were calculated to yield S/N ratios of 100–200 at Ca II K. The last column of Table 1 gives the total exposure time achieved for each target. Individual exposures were limited to 30 minutes to minimize the effects of cosmic ray hits during the integrations. Standard calibration exposures (biases and flats) were obtained at the beginning of each night, while Th-Ar comparison lamp exposures were obtained throughout the night at intervals of 2–3 hours. From the widths of Th I emission lines in the comparison spectra, we find that the actual resolving power during our observing run was $R \approx 66,000$, corresponding to a velocity resolution of $\sim 4.5 \text{ km s}^{-1}$. To aid in the removal of telluric absorption lines, particularly near the Na I D doublet and the K I $\lambda 7698$ line, a bright, unreddened star (e.g., α Peg) was observed each night along with the science targets.

The raw science exposures were reduced following standard procedures within the IRAF environment. The average bias frame was subtracted from the flats and science exposures and from the comparison lamp frames. Cosmic rays were then removed from the science and Th-Ar exposures. Cosmic rays were effectively removed from the flats by taking the median of all the flats obtained on a given night. Scattered light was subtracted from the median flat and from the science exposures in both the dispersion and cross-dispersion directions. Unfortunately, the flat lamp in use with the Tull spectrograph exhibits emission features at the locations of the Na I D lines. Thus, we extracted one-dimensional spectra from the scattered-light corrected flats in order to remove these emission features. One-dimensional spectra were also extracted from the science and Th-Ar exposures, and the corrected flat spectra were divided into the science and comparison lamp spectra. We also performed a traditional two-dimensional flat-fielding to check that there was essentially no difference between the two procedures (outside the regions affected by the Na I emission features).

Wavelength solutions were obtained by identifying emission lines in the Th-Ar comparison spectra. After applying the wavelength solutions to the science spectra, the next step is to correct for telluric absorption near the Na I and K I lines. A template for telluric absorption was created from our observations of the unreddened standard star. This template was then divided into the science spectra, after correcting for differences in airmass and for small shifts in the dispersion direction. This procedure is very effective at removing relatively weak telluric absorption features from the regions surrounding the Na I D₁ and D₂ lines and the K I $\lambda 7698$ line. The stronger member of the K I doublet at 7664.9 \AA coincides with a strong atmospheric O₂ absorption line and therefore could not be recovered. Lastly, the

science spectra were shifted to the LSR frame of reference and the multiple exposures of a given target were co-added to produce final high S/N ratio spectra. Typical S/N ratios are ~ 150 at Ca II K and ~ 215 at Na I D.

3 ANALYSIS

3.1 Separating stellar from interstellar absorption

For many of our targets, the process of separating stellar absorption from interstellar absorption was straightforward. BD+31 4218 is an early B-type (emission-line) star with a projected rotational velocity of $\sim 300 \text{ km s}^{-1}$. Three other targets, HD 335153, BD+31 4224, and BD+31 4256, are late B dwarfs or subgiants with rotationally broadened absorption lines. These stars have $v \sin i \gtrsim 200 \text{ km s}^{-1}$ (see Appendix A). In each of these cases, narrow interstellar absorption lines (e.g., Ca II H and K) are superimposed onto very broad stellar absorption features. Thus, the interstellar absorption profiles were normalized simply by fitting low-order Legendre polynomials to the smoothly varying stellar spectra.

Two of our targets, HD 198301 and HD 335334, exhibit narrow stellar absorption lines (with $v \sin i \approx 20 \text{ km s}^{-1}$). Thus, the process of separating stellar absorption from interstellar absorption was much more difficult in these cases. This difficulty is what prompted us to attempt to derive accurate spectral classifications for our program stars. At the beginning of our investigation, the spectral types listed in SIMBAD for four of our targets (HD 335153, HD 198301, BD+31 4256, and HD 335334) were “A0” (with no luminosity class given). BD+31 4218 had the classification “B2”. Fesen et al. (2018a) classified BD+31 4224 as a B7 IV-V star. We sought to improve upon these classifications so that we could correctly identify any stellar absorption that may be impacting the interstellar lines, particularly toward HD 198301 and HD 335334. Most of the details regarding our derivations of spectral types and luminosity classes for our program stars are presented in Appendix A. Here, we focus specifically on the results for HD 198301 and HD 335334.

3.1.1 HD 198301 — a late B subgiant

The procedure described in Appendix A yields a spectral type of B8 IV for HD 198301. We investigated the accuracy of this classification further using the high-resolution synthetic stellar spectra provided by Munari et al. (2005). The effective temperature of a B8 subgiant is expected to be $T_{\text{eff}} \approx 12,000 \text{ K}$, while the surface gravity should be approximately $\log g \approx 3.9$ (Schmidt-Kaler 1982). In Figure 2, we show a comparison between the observed spectrum of HD 198301

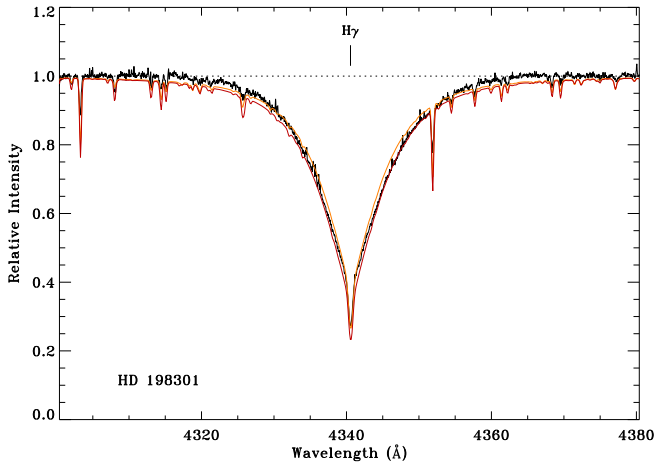


Figure 2. Continuum normalized spectrum of HD 198301 in the vicinity of the stellar H γ line. Model stellar spectra (colored curves) are shown superimposed onto the observed spectrum (black curve). The models correspond to $T_{\text{eff}} = 12,000$ K (red) and $13,000$ K (orange), with $\log g = 3.5$ in both cases.

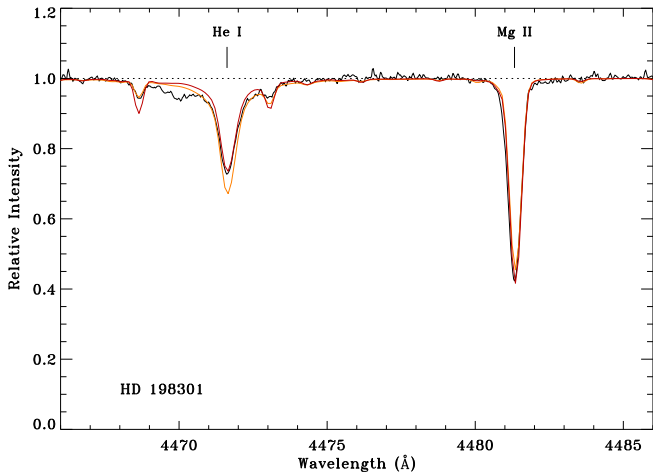


Figure 3. Continuum normalized spectrum of HD 198301 in the vicinity of the stellar He I $\lambda 4471$ and Mg II $\lambda 4481$ lines. Model stellar spectra (colored curves) are shown superimposed onto the observed spectrum (black curve). The models correspond to $T_{\text{eff}} = 12,000$ K (red) and $13,000$ K (orange), with $\log g = 3.5$ in both cases.

in the vicinity of the stellar H γ line and two synthetic stellar spectra. The model spectra correspond to $T_{\text{eff}} = 12,000$ K (red curve) and $13,000$ K (orange curve), with $\log g = 3.5$ in both cases. (The models have been Doppler-shifted by 9 km s^{-1} to match the radial velocity of HD 198301.) Both models yield a relatively good fit to the data, although the higher temperature model has an H γ line that is somewhat too narrow. (There is a slight mismatch in the wings of the line very far from the core. This is probably due to continuum placement errors. The Balmer lines generally span multiple echelle orders in our high-resolution spectra, making continuum placement challenging. However, this should not affect the widths of the lines closer to the core.)

In Figure 3, we show the same two model stellar spectra compared with the observed spectrum of HD 198301 in the vicinity of the stellar He I $\lambda 4471$ and Mg II $\lambda 4481$ lines. The He I $\lambda 4471$ /Mg II $\lambda 4481$ line ratio is one of the main criteria used for temperature classification

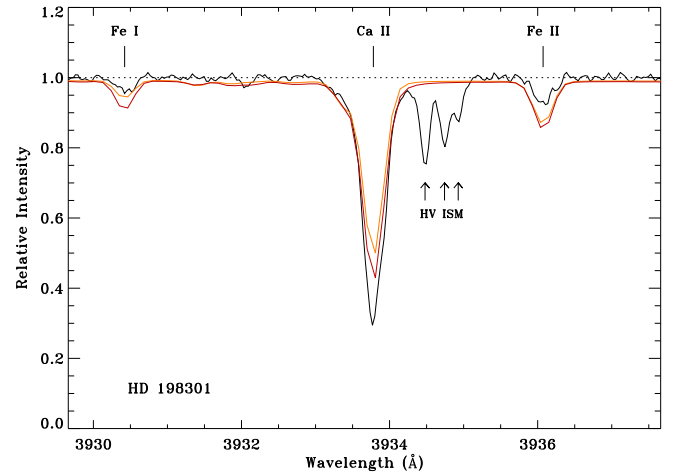


Figure 4. Continuum normalized spectrum of HD 198301 in the vicinity of the Ca II K line. Model stellar spectra (colored curves) are shown superimposed onto the observed spectrum (black curve). The models correspond to $T_{\text{eff}} = 12,000$ K (red) and $13,000$ K (orange), with $\log g = 3.5$ in both cases. Three high-velocity interstellar Ca II absorption features are identified.

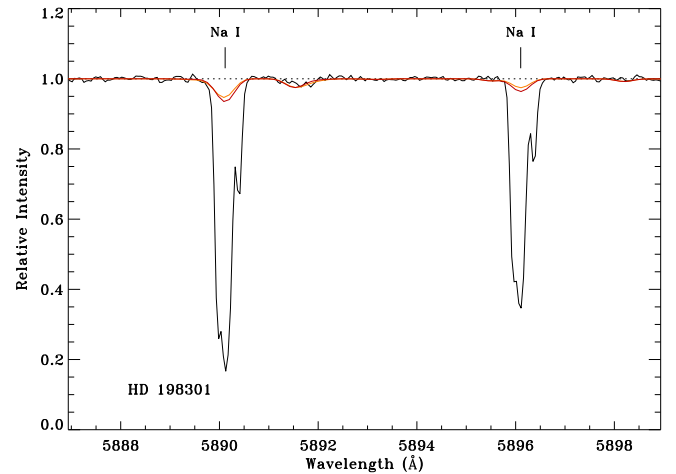


Figure 5. Continuum normalized spectrum of HD 198301 in the vicinity of the Na I D lines. Model stellar spectra (colored curves) are shown superimposed onto the observed spectrum (black curve). The models correspond to $T_{\text{eff}} = 12,000$ K (red) and $13,000$ K (orange), with $\log g = 3.5$ in both cases. Most of the Na I absorption is interstellar.

in late B-type stars (e.g., [Gray & Corbally 2009](#)). The good fit of the synthetic spectrum with $T_{\text{eff}} = 12,000$ K helps to firmly establish a temperature class of B8 for HD 198301. We note that a good match between the synthetic spectrum with $T_{\text{eff}} = 12,000$ K and $\log g = 3.5$ and the observed spectrum of HD 198301 is found for other important stellar absorption lines, such as He I $\lambda 4026$, Si II $\lambda 4128, 4130$, and He I $\lambda 4921$.

Having established a best-fitting stellar model for HD 198301, we turned our attention to the Ca II K and Na I D lines, where contributions from interstellar absorption lines are expected. Figure 4 shows the Ca II K region. The observed Ca II K feature is deeper than either of the two synthetic models would predict, suggesting that some of this absorption may be due to interstellar Ca II at low velocity. More striking, however, are the three narrow redshifted absorption features that fall between the strong Ca II K line and a nearby Fe II line. The synthetic models have no absorption lines at

these wavelengths. We therefore attribute these absorption features to high-velocity interstellar Ca II K components. The three components have LSR velocities of +62, +82, and +96 km s⁻¹. Our interpretation of these absorption features is confirmed by the fact that the three components are detected at the same velocities in the nearby Ca II H line. (The components are somewhat harder to discern at Ca II H because they appear on the steeply decreasing edge of the stellar He I line. Nevertheless, the reality of the components appears to be firmly established.)

The Na I D region of the HD 198301 spectrum is shown in Figure 5. Here, it is obvious that most of the absorption in the Na I D lines is from interstellar Na I. The Na I lines in both of the model stellar spectra are significantly weaker than the observed lines. Moreover, the observed Na I absorption profiles show a clear component structure of intrinsically narrow features, indicating an origin in cold, interstellar clouds. The high-velocity components seen in the Ca II H and K lines are not detected in Na I. However, this is not surprising since high-velocity gas components associated with SNRs often have very low Na I/Ca II ratios (e.g., Danks & Sembach 1995; Sallmen & Welsh 2004; Ritchey 2020), a consequence of the return of Ca⁺ ions to the gas phase following the destruction of interstellar dust grains in SNR shocks.

Before proceeding with the analysis of the interstellar Ca II H and K profiles and the Na I D profiles toward HD 198301, the observed spectra for those regions were divided by the best-fitting model spectrum (i.e., the model with $T_{\text{eff}} = 12,000$ K and $\log g = 3.5$) in order to remove the contributions from stellar absorption lines. This procedure had little effect on the interstellar Na I D profiles or on the high-velocity Ca II components. However, the low-velocity interstellar Ca II absorption toward HD 198301 is severely impacted by stellar absorption and the removal of this contaminating absorption is model-dependent. While we have chosen the best stellar model available, there remains some uncertainty about the strength of the interstellar Ca II line at low velocity.

3.1.2 HD 335334 — a double-line spectroscopic binary

Initially, our high-resolution spectrum of HD 335334 was difficult to interpret. There appeared to be many more narrow stellar absorption lines than would be expected for a late B or early A dwarf or subgiant. Upon closer examination, it became clear that each of the major stellar absorption lines had a corresponding line at a fixed velocity from the primary line. We thus suspected that the star was a double-line spectroscopic binary. Fortunately, this star had been observed on two consecutive nights during the six night observing run. Two 30 minute exposures of HD 335334 were obtained on 2022 Sep. 4, and six 30 minute exposures were obtained on Sep. 5. (UT dates are quoted.) We therefore created summed spectra for each night separately to see if there was any shift in the stellar absorption lines from one night to the next.

In Figure 6, we show the separate summed spectra of HD 335334 from the two consecutive nights for the spectral region containing the Na I D lines. The spectrum from Sep. 4 (plotted with a red line) has a lower S/N ratio due to the lower total exposure time. Nevertheless, it is clear that the stellar Na I lines (labelled “A” and “B” in the figure) shifted significantly between the two observations, while the two narrow interstellar Na I components remained stationary. In the spectrum acquired on Sep. 4, the radial velocities of the stellar Na I lines are -37 km s⁻¹ for component A and $+113$ km s⁻¹ for component B. In the Sep. 5 spectrum, the velocities are -17 km s⁻¹ for component A and $+88$ km s⁻¹ for component B. Thus, the velocity shift for component A is ~ 20 km s⁻¹ (to the red), while the shift for

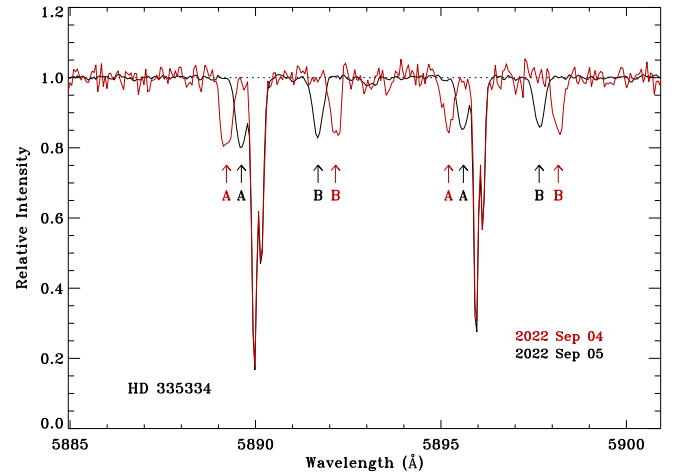


Figure 6. Continuum normalized spectra of HD 335334 in the vicinity of the Na I D lines from observations obtained on two consecutive nights: 2022 Sep. 4 (red) and Sep. 5 (black). The stellar Na I D lines of the primary component (“A”) and the secondary component (“B”) of the spectroscopic binary can be seen to shift from one night to the next, while the interstellar Na I D lines are stationary.

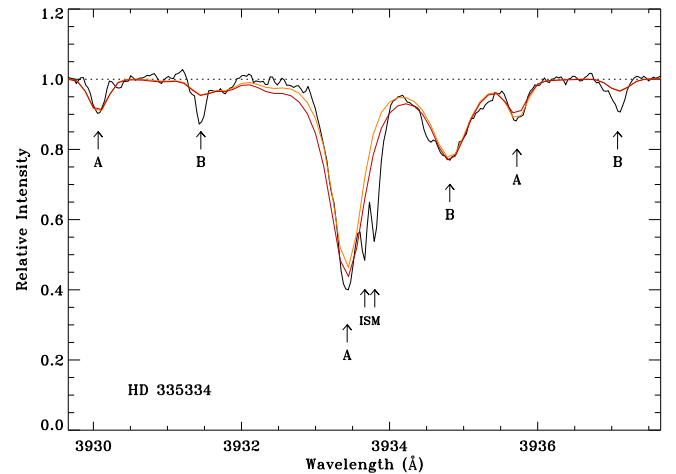


Figure 7. Continuum normalized spectrum of HD 335334 in the vicinity of the Ca II K line from our observations obtained on 2022 Sep. 5. Model stellar spectra (colored curves) are superimposed onto the observed spectrum (black curve). The models show composite stellar spectra, with $T_{\text{eff}} = 10,500$ K for both the primary component (“A”) and the secondary component (“B”). The red curve adopts $\log g = 4.0$ for both the primary and the secondary, while the orange curve adopts $\log g = 3.5$ for the primary and $\log g = 4.0$ for the secondary. Two low-velocity interstellar Ca II components are identified. These are the same two interstellar components that can be seen in the Na I D lines in Figure 6.

component B is ~ 25 km s⁻¹ (to the blue). The slightly smaller shift for component A indicates that this star has a somewhat higher mass (hence the designation as component “A”).

The Ca II K region of the Sep. 5 spectrum of HD 335334 is shown in Figure 7. Two synthetic model spectra are also shown in the plot. The model spectra were constructed from the high-resolution synthetic spectra provided by Munari et al. (2005). However, in this case, we created composite spectra to compare with the observations. The procedure described in Appendix A yields a spectral type of B9

V for HD 335334.¹ A B9 V star is expected to have an effective temperature of $T_{\text{eff}} \approx 10,500$ K and a surface gravity of $\log g \approx 4.0$ (Schmidt-Kaler 1982). Thus, we created a composite spectrum from two synthetic model spectra, both with $T_{\text{eff}} = 10,500$ K and $\log g = 4.0$. We Doppler-shifted the model spectra in accordance with the observed radial velocities of the two components. We then divided the flux of the model for component B by 2.5 and summed the two model spectra together to produce a composite spectrum. The normalized version of this composite spectrum is shown by the red curve in Figure 7. The factor of 2.5 was determined by trial-and-error to match the observed ratio of the Ca II K lines from components A and B (see Figure 7). This same ratio between A and B is seen in several other prominent absorption lines in the spectrum of HD 335334 and may indicate that the luminosity of component A is ~ 2.5 times larger than that of component B. Given the prospect of a higher luminosity for component A, we created another composite model spectrum with all of the same parameters as the first model except the surface gravity of the primary component was changed to $\log g = 3.5$. This alternative composite spectrum is shown by the orange curve in Figure 7.

The purpose of creating the composite spectra discussed above was not to attempt to match the observed spectrum of HD 335334 perfectly. The main purpose was to correctly identify stellar absorption features particularly in the vicinity of the Ca II H and K lines, so that the interstellar Ca II absorption features could be properly identified and analyzed. As can be seen in Figure 7, much of the absorption in the Ca II K region of the HD 335334 spectrum arises from stellar lines. The strongest feature is the Ca II K line from the primary star. The secondary Ca II K line is the other broad absorption feature redshifted by 105 km s^{-1} relative to the primary. Two other pairs of stellar lines can be seen in the figure. These are the Fe I $\lambda 3930$ and Fe II $\lambda 3935$ lines that are also seen in the spectrum of HD 198301 (Figure 4). Two narrow interstellar Ca II components can be seen on the red side of the primary Ca II K line. These are the same two low-velocity interstellar components that can be seen in the Na I D lines toward HD 335334 (Figure 6). After accounting for stellar absorption lines, we find no evidence of high-velocity interstellar Na I or Ca II components toward HD 335334.

Fesen et al. (2018b) claimed to detect high-velocity interstellar Na I and Ca II components toward HD 335334 (a star that those authors refer to as “Star X”). They reported finding a blueshifted component in Na I and Ca II at approximately -60 km s^{-1} and a redshifted component near $+90 \text{ km s}^{-1}$. However, considering the analysis presented above, it is now clear that the “blue” and “red” components discussed by Fesen et al. (2018b) are not high-velocity interstellar components. They are the stellar Na I and Ca II components from the primary and secondary stars that constitute the spectroscopic binary. Note that the “red” component discussed by Fesen et al. (2018b) is the primary and the “blue” component is the secondary. This can be seen in their Figure 3, which shows that the Ca II absorption is much stronger in the red component compared to the blue component. Clearly, Fesen et al. (2018b) observed HD 335334 at a different orbital phase compared to our observations.

Before proceeding with the analysis of the interstellar Na I and Ca II lines toward HD 335334, we removed the surrounding stellar

absorption features. In this case, we did not use the model stellar spectra to divide out the stellar absorption (because the models are not a perfect match to the observed spectrum). Instead, we manually removed the obvious stellar absorption features. For the Na I lines, this was not a problem because the interstellar Na I lines are much stronger than the stellar lines. For the Ca II H and K lines, where the interstellar features are blended with stellar absorption from the primary, we did our best to deblend the various features. Nevertheless, there remains some uncertainty about the strength of the low-velocity interstellar Ca II components toward HD 335334.

3.2 Profile fitting

After removing any contaminating stellar absorption from the interstellar absorption profiles toward our targets, the interstellar lines were analyzed using a multi-component Voigt profile fitting routine known as ISMOD (Sheffer et al. 2008). The profile synthesis code derives the best-fitting column density, velocity, and Doppler b -value of each individual interstellar component through a simple root mean square minimizing procedure. An additional constraint for the Na I and Ca II analyses is that the two lines of the doublet (Na I D₁ and D₂ and Ca II H and K) were fit simultaneously so that a single set of component parameters is obtained for each doublet. While our spectra have moderately high resolution ($\sim 4.5 \text{ km s}^{-1}$), we are likely still not resolving the individual interstellar absorption components. High and ultra-high resolution studies of interstellar lines have revealed that the intrinsic widths of Ca II components are typically in the range 1 to 3 km s^{-1} (e.g., Welty et al. 1996; Pan et al. 2005), while Na I components often have intrinsic b -values that are $\sim 1 \text{ km s}^{-1}$ or less (e.g., Welty et al. 1994). A simultaneous fit to both members of the Na I and Ca II doublets can thus help to mitigate the effect on the derived column densities of unresolved saturation in the line profiles (particularly for the Na I lines).

For most of our target sight lines, the only strong interstellar absorption features detected are the Na I D and Ca II H and K lines. In some cases, a weak K I $\lambda 7698$ feature is also detected. This is consistent with the low reddening seen toward most of our stars (Table 1). With the exception of BD+31 4218, the values of $E(B-V)$ for our sight lines are ~ 0.1 or less, consistent with the value of 0.08 typically quoted for the Cygnus Loop (e.g., Raymond et al. 1981; Fesen et al. 1982). The reddening toward BD+31 4218, however, is ~ 0.3 . This star has the largest distance among the stars in our sample (~ 1100 pc) and is located somewhat beyond the bright optical emission features to the northwest of the Cygnus Loop (see Figure 1). Fesen et al. (2018a,b) demonstrated that the region of the sky immediately beyond the western limb of the Cygnus Loop is characterized by a sharp increase in dust extinction, consistent with our finding a higher value of $E(B-V)$ toward BD+31 4218. Several other atomic and molecular absorption lines are detected toward BD+31 4218, including Li I $\lambda 6707$, Ca I $\lambda 4226$, CH $\lambda 4300$, CH⁺ $\lambda 4232$, and CN $\lambda 3874$. These lines likely arise from material associated with the western molecular cloud that Fesen et al. (2018b) suggested may be interacting with the Cygnus Loop.

Figure 8 presents our simultaneous profile synthesis fits to the Na I and Ca II lines toward BD+31 4218. Because the Na I D lines are heavily saturated in this direction, we first fit the K I $\lambda 7698$ line independently. (This fit is shown in the top panel of Figure 8.) We then held the fractional column densities and relative velocities of the three K I components fixed in our simultaneous fit to the Na I D lines. The resulting $N(\text{Na I})/N(\text{K I})$ ratio of ~ 80 for the line of sight is consistent with the ratios that characterize typical diffuse molecular cloud sight lines (e.g., Welty & Hobbs 2001).

¹ The procedure we use for classifying our stars is based on an analysis of the spectra after smoothing the data to a resolution of 1.8 \AA (see Appendix A). At such a low resolution, the two components of the spectroscopic binary cannot be discerned. Thus, the spectral type we derive for HD 335334 refers to the composite system only.

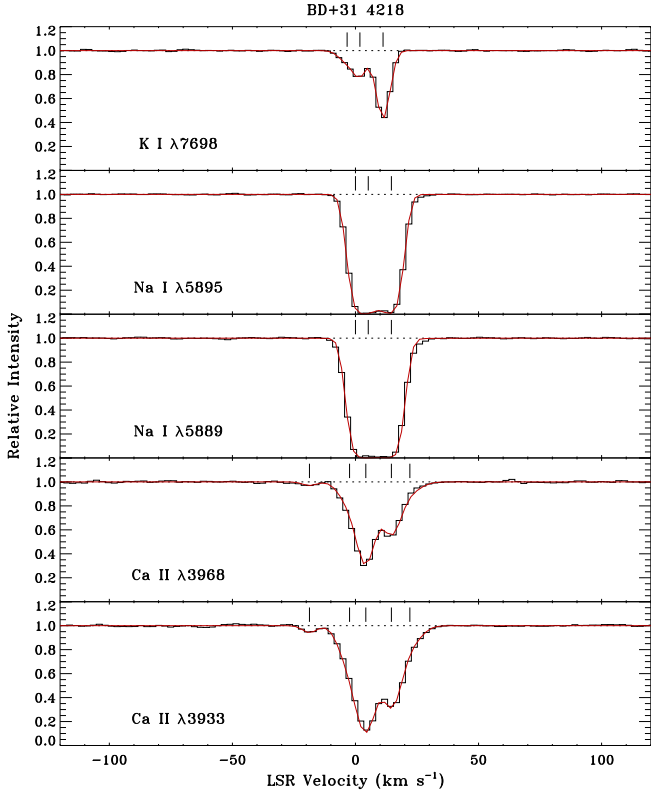


Figure 8. Simultaneous profile synthesis fits to the interstellar Na I D₁ and D₂ lines and the Ca II H and K lines toward BD+31 4218. An independent fit to the K I $\lambda 7698$ line is also shown. Synthetic absorption profiles (red curves) are shown superimposed onto the observed spectra (black histograms). Tick marks give the positions of the individual components included in the fits.

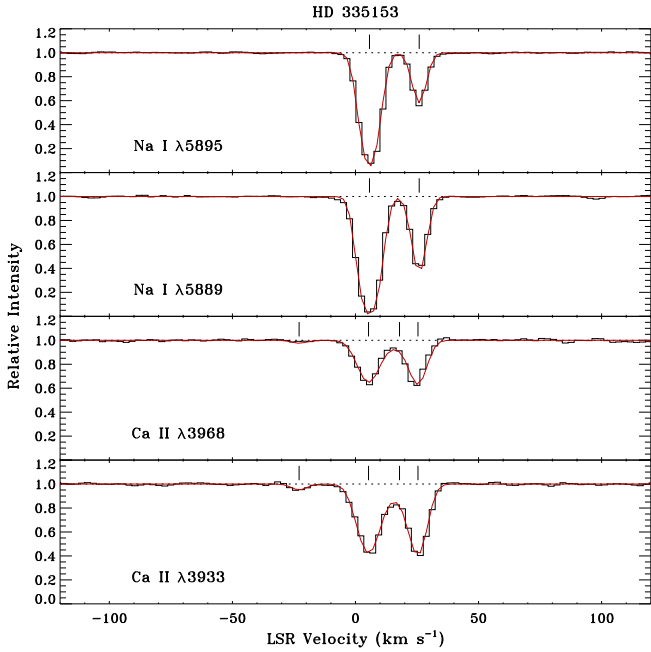


Figure 9. Simultaneous profile synthesis fits to the interstellar Na I D₁ and D₂ lines and the Ca II H and K lines toward HD 335153. Synthetic absorption profiles (red curves) are shown superimposed onto the observed spectra (black histograms). Tick marks give the positions of the individual components included in the fits.

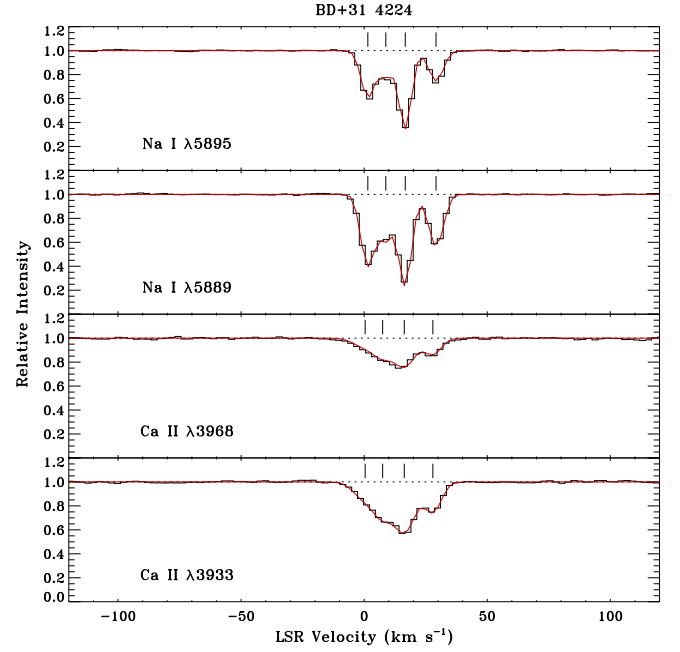


Figure 10. Simultaneous profile synthesis fits to the interstellar Na I D₁ and D₂ lines and the Ca II H and K lines toward BD+31 4224. Synthetic absorption profiles (red curves) are shown superimposed onto the observed spectra (black histograms). Tick marks give the positions of the individual components included in the fits.

Our simultaneous profile synthesis fits to the interstellar Na I D and Ca II H and K lines toward the other five targets are presented in Figures 9 through 13. In general, these sight lines show much weaker Na I and Ca II absorption features and the process of fitting the absorption profiles did not present any unusual complications. We did strive to include Na I and Ca II components at similar velocities for a given sight line so that the $N(\text{Na I})/N(\text{Ca II})$ ratios of the different components could be analyzed in a consistent manner. Again, at a velocity resolution of $\sim 4.5 \text{ km s}^{-1}$, we are likely not fully resolving the detailed interstellar component structure toward our targets. Nevertheless, given the general weakness of the absorption lines, and our procedure of simultaneously fitting both lines of the Na I and Ca II doublets, the column densities we derive should not be significantly impacted.

Table 2 presents the total equivalent widths and column densities of the interstellar atomic and molecular lines detected toward our sample of stars. The equivalent width errors reflect uncertainties due to noise in the continuum as well as errors due to continuum placement. The column density errors include an additional term related to the level of saturation in the absorption line. As anticipated, the Na I column density toward BD+31 4218 is more than an order of magnitude larger than toward the other targets. Comparisons of the total (line-of-sight) column densities of the atomic and molecular species observed toward BD+31 4218 (e.g., Na I vs. K I, Li I vs. Na I and K I, and CH vs. Na I and K I) all show very good agreement with typical Galactic relationships (Welty & Hobbs 2001; Welty et al. 2006). The $N(\text{Na I})$ and $N(\text{K I})$ values then imply a total hydrogen column density of $\log N(\text{H}_{\text{tot}}) \sim 21.3$ toward BD+31 4218 (Welty & Hobbs 2001). Likewise, the column densities of Na I, K I, and CH imply a molecular hydrogen column density of $\log N(\text{H}_2) \sim 20.8$ and a molecular fraction of $f(\text{H}_2) = 2N(\text{H}_2)/N(\text{H}_{\text{tot}}) \sim 0.6$ (Welty & Hobbs 2001; Sheffer et al. 2008). For the other five sight lines, the Na I and K I column densities imply total hydrogen column densities in the

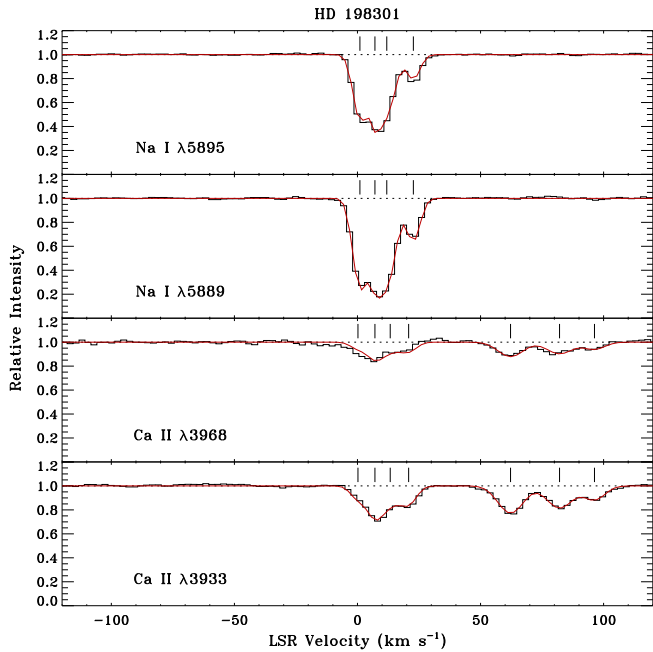


Figure 11. Simultaneous profile synthesis fits to the interstellar Na I D₁ and D₂ lines and the Ca II H and K lines toward HD 198301. Synthetic absorption profiles (red curves) are shown superimposed onto the observed spectra (black histograms). Tick marks give the positions of the individual components included in the fits. Note the high-velocity Ca II components at +62, +82, and +96 km s⁻¹.

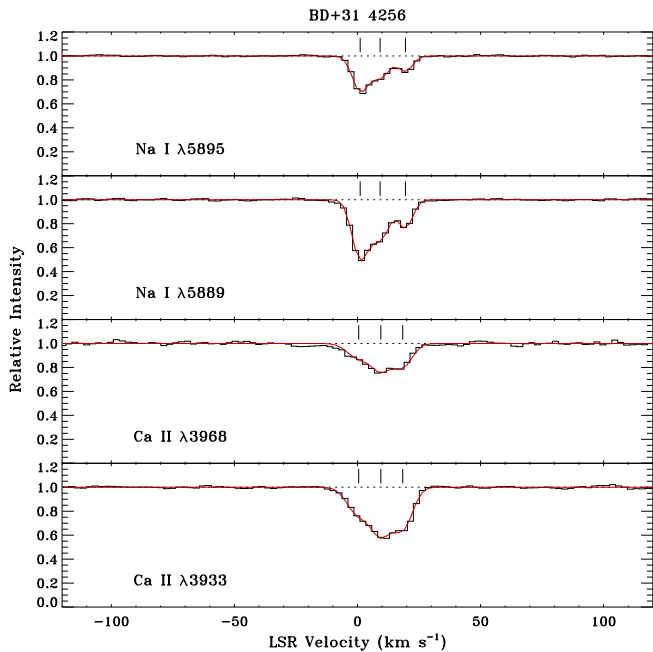


Figure 12. Simultaneous profile synthesis fits to the interstellar Na I D₁ and D₂ lines and the Ca II H and K lines toward BD+31 4256. Synthetic absorption profiles (red curves) are shown superimposed onto the observed spectra (black histograms). Tick marks give the positions of the individual components included in the fits.

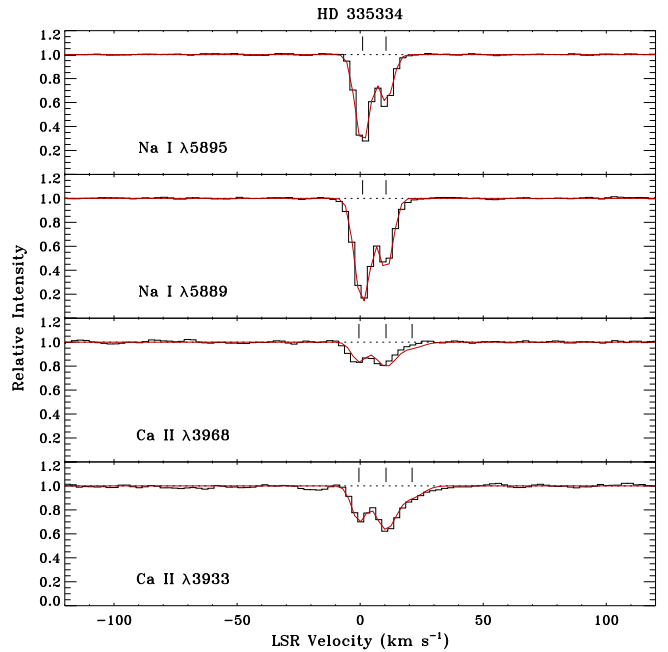


Figure 13. Simultaneous profile synthesis fits to the interstellar Na I D₁ and D₂ lines and the Ca II H and K lines toward HD 335334. Synthetic absorption profiles (red curves) are shown superimposed onto the observed spectra (black histograms). Tick marks give the positions of the individual components included in the fits.

range $\log N(\text{H}_{\text{tot}}) \sim 20.4\text{--}20.8$ and molecular hydrogen fractions of $f(\text{H}_2) \sim 0.1$.

Details regarding the individual Na I and Ca II components discerned through our profile fitting analysis are presented in Table 3. For each component, we list the LSR velocities, column densities, and b -values of Na I and Ca II, along with the $N(\text{Na I})/N(\text{Ca II})$ ratio. In cases where only Ca II is detected, 3σ upper limits on $N(\text{Na I})$ and $N(\text{Na I})/N(\text{Ca II})$ are reported. Considering the resolution of our data, the velocities of the corresponding Na I and Ca II components show good agreement. The median absolute difference in velocity between Na I and Ca II is 0.9 km s^{-1} . The Ca II components are broader, with an average b -value of 4.5 km s^{-1} (identical to the velocity resolution). The average b -value of the Na I components is 2.6 km s^{-1} . The Na I/Ca II column density ratios exhibit a wide range. For components with Na I detections, the $N(\text{Na I})/N(\text{Ca II})$ ratios range from ~ 0.3 to ~ 50 , with higher ratios generally associated with larger Na I column densities. For components with Ca II detections only, the upper limits on $N(\text{Na I})/N(\text{Ca II})$ are ~ 0.2 or less. Of particular note are the three high-velocity Ca II components toward HD 198301, which exhibit very low upper limits on $N(\text{Na I})/N(\text{Ca II})$.

Further details regarding the atomic and molecular component structure along the line of sight to BD+31 4218 are provided in Table 4. The strongest Na I and K I component has a velocity of approximately $+13 \text{ km s}^{-1}$. This is also the strongest component in CH and the only component detected in CN absorption. The $N(\text{Na I})/N(\text{Ca II})$ ratio for this component (~ 50) is the largest in our sample. The $N(\text{K I})/N(\text{Ca I})$ ratio for the $+13 \text{ km s}^{-1}$ component is also rather high (~ 80). Taken together, the high values for these two ratios indicate substantial depletion of Ca onto interstellar dust grains. The detection of strong CN and CH absorption, and the lack of CH⁺ absorption at the same velocity, is a further indication of the presence of dense gas (e.g., Pan et al. 2005; Sheffer et al. 2008).

Three CN transitions are detected toward BD+31 4218: the $R(0)$,

Table 2. Total equivalent widths (in mÅ) and column densities (in cm⁻²) of the atomic and molecular species observed toward the program stars. The three CN lines listed toward BD+31 4218 are (in order of increasing wavelength) the *R*(1), *R*(0), and *P*(1) lines of the *B*–*X* (0, 0) band.

Star	Species	λ (Å)	W_λ (mÅ)	$\log N$
BD+31 4218	Li I	6707.826	1.9 ± 0.6	9.81 ± 0.12
	Na I	5889.951	491.3 ± 0.6	14.02 ± 0.07
		5895.924	473.8 ± 0.7	14.02 ± 0.07
		7698.965	155.7 ± 1.0	12.11 ± 0.03
	Ca I	4226.728	8.9 ± 0.8	10.51 ± 0.04
	Ca II	3933.661	251.5 ± 1.2	12.74 ± 0.03
		3968.467	170.8 ± 1.4	12.74 ± 0.02
	CH	4300.313	19.8 ± 0.5	13.42 ± 0.02
	CH ⁺	4232.548	5.1 ± 0.7	12.78 ± 0.05
	CN	3873.994	5.9 ± 0.5	12.33 ± 0.04
3874.602		18.4 ± 0.6	12.67 ± 0.02	
3875.758		4.1 ± 0.8	12.33 ± 0.07	
HD 335153	Na I	5889.951	311.5 ± 1.0	12.86 ± 0.07
		5895.924	261.0 ± 1.0	12.86 ± 0.06
	K I	7698.965	18.6 ± 0.9	11.04 ± 0.02
	Ca II	3933.661	181.5 ± 1.5	12.46 ± 0.02
3968.467		98.9 ± 1.6	12.46 ± 0.01	
BD+31 4224	Na I	5889.951	292.8 ± 0.9	12.55 ± 0.05
		5895.924	209.4 ± 0.9	12.55 ± 0.04
	K I	7698.965	5.5 ± 0.7	10.50 ± 0.05
Ca II	3933.661	134.6 ± 1.2	12.28 ± 0.01	
	3968.467	79.5 ± 1.8	12.28 ± 0.01	
	HD 198301	Na I	5889.951	325.8 ± 1.0
5895.924			236.4 ± 1.1	12.59 ± 0.02
Ca II		3933.661	155.4 ± 2.0	12.30 ± 0.01
		3968.467	83.6 ± 3.9	12.30 ± 0.02
BD+31 4256	Na I	5889.951	169.8 ± 1.2	12.05 ± 0.02
		5895.924	98.9 ± 1.3	12.05 ± 0.01
	Ca II	3933.661	124.8 ± 1.6	12.26 ± 0.01
		3968.467	71.5 ± 2.5	12.26 ± 0.02
HD 335334	Na I	5889.951	214.7 ± 0.7	12.50 ± 0.06
		5895.924	165.7 ± 0.8	12.50 ± 0.04
	K I	7698.965	15.7 ± 1.1	10.97 ± 0.03
	Ca II	3933.661	93.5 ± 2.3	12.10 ± 0.02
3968.467		47.9 ± 1.7	12.10 ± 0.02	

R(1), and *P*(1) lines within the *B*–*X* (0, 0) band near 3874 Å (see Table 2). To analyze these features, we used a modified version of the profile fitting routine, which performs a simultaneous fit to the three CN transitions, keeping the velocities and *b*-values consistent among the three lines. The column density in the *N* = 0 rotational level is determined from the *R*(0) line, while the *N* = 1 column density is derived from the *R*(1) and *P*(1) lines simultaneously. This procedure yields a *b*-value of 2.1 km s⁻¹, similar to the *b*-values we find for Na I (2.4 km s⁻¹) and K I (2.3 km s⁻¹) for the same velocity component. The individual rotational column densities are $\log N(N = 0) = 12.67 \pm 0.02$ and $\log N(N = 1) = 12.33 \pm 0.03$. Thus, the rotational excitation temperature is $T_{01}(\text{CN}) = 2.90 \pm 0.15$ K. This result is consistent with excitation by the cosmic microwave background at a temperature of 2.725 K, but may also be indicative of a mild excess due to additional excitation by electron impact (e.g., Ritchey et al. 2011).

3.3 Comparison with the survey by Welsh et al. (2002)

The only previous high-resolution study of interstellar lines toward stars in the Cygnus Loop region is that of Welsh et al. (2002). These authors studied Na I and Ca II lines toward nine stars with projected on-sky positions within or near the Cygnus Loop SNR. At the time of their observations, the distances to the targets in Welsh et al. (2002) were not very well determined (and the targets were selected assuming the distance to the Cygnus Loop was 440 pc; Blair et al. 1999). Now, with the advent of accurate distances provided by the Gaia satellite, we can reevaluate the results of Welsh et al. (2002) and compare their results to those of our investigation. Most of the Welsh et al. (2002) targets have Gaia EDR3 distances that are less than ~630 pc. These include HD 198597 (213⁺²₋₁ pc), HD 198056 (310⁺³₋₃ pc), HD 198197 (392⁺⁷₋₆ pc), HD 198946 (445⁺¹³₋₂₀ pc), HD 199102 (536⁺⁸₋₈ pc), HD 199042 (594⁺¹⁰₋₁₀ pc), and HD 335212 (626⁺⁶₋₇ pc). (Distances from Bailer-Jones et al. (2021) are given in parentheses.) Only two of the Welsh et al. (2002) stars have distances greater than 700 pc. These are HD 198301 (872⁺²¹₋₂₀ pc), which is also a target in our investigation, and HD 197702 (1072⁺³¹₋₂₆ pc). All of our targets have Gaia EDR3 distances that are greater than ~700 pc (Table 1). Thus, by combining the Welsh et al. (2002) survey with our own, we can examine how the nature of the interstellar absorption changes as a function of distance toward the Cygnus Loop SNR.

The two closest stars in the Welsh et al. (2002) sample exhibit only a single velocity component in Na I and Ca II at an LSR velocity near 0 km s⁻¹, consistent with local foreground material. The Welsh et al. (2002) stars with distances greater than ~350 pc generally exhibit multiple Na I and Ca II components with average LSR velocities of +1, +9, +19, and +30 km s⁻¹. These velocities are very similar to the velocities of the Na I and Ca II components seen toward our targets (with the exception of the three high-velocity Ca II components detected toward HD 198301). Since the range of absorption velocities is similar between the relatively nearby stars (at distances between ~390 pc and ~630 pc) and the stars that are further away (at distances greater than ~700 pc), it is difficult to determine whether any of the low velocity components toward our stars might be associated with the Cygnus Loop SNR. At the longitude of the Cygnus Loop (~74°) and at the distance of the furthest star in our sample (~1100 pc), any gas participating in differential Galactic rotation would be expected to have an LSR velocity between 0 and +7 km s⁻¹. Velocities well outside of this range might then be considered peculiar. For example, many of our targets exhibit gas components with velocities between +20 and +30 km s⁻¹. However, while it might be tempting to ascribe this material to the effects of low velocity shocks associated with the Cygnus Loop, similar velocities are seen toward stars that are likely much closer than the SNR.

The only definitive conclusion we can reach in this regard is that the star HD 198301 must lie behind the Cygnus Loop SNR. Of the 14 stars in the combined sample of Welsh et al. (2002) and this paper, HD 198301 is the only star that exhibits truly high-velocity interstellar absorption. Indeed, our detection of Ca II absorption approaching 100 km s⁻¹ toward HD 198301 is the first conclusive detection of high-velocity, low-ionization gas associated with the Cygnus Loop. Curiously, HD 198301 was also observed by Welsh et al. (2002). However, they make no mention of any high-velocity gas. (Their plot of the Ca II spectrum in this direction extends to only ±40 km s⁻¹.) Thus, either the high-velocity features were not present in the spectrum obtained by Welsh et al. (2002) or those authors mistook these features for narrow stellar lines or for noise in the spectrum (B. Welsh, 2023, private communication). Dramatic temporal variations in Na I and/or Ca II lines have been seen toward numerous stars in the Vela

Table 3. Velocities (in km s^{-1}), column densities (in cm^{-2}), and b -values (in km s^{-1}) of the individual Ca II and Na I absorption components discerned through profile fitting. Upper limits on $N(\text{Na I})$ are provided in cases where Ca II is detected but Na I is not. The last column gives the $N(\text{Na I})/N(\text{Ca II})$ ratio (or upper limit on the ratio).

Star	$v_{\text{LSR}}(\text{Ca II})$	$\log N(\text{Ca II})$	$b(\text{Ca II})$	$v_{\text{LSR}}(\text{Na I})$	$\log N(\text{Na I})$	$b(\text{Na I})$	$N(\text{Na I})/N(\text{Ca II})$
BD+31 4218	-18.7	10.81 ± 0.04	2.7	...	<9.8	...	<0.10
	-2.4	11.78 ± 0.01	4.8	+0.0	12.98 ± 0.06	2.2	16.0 ± 2.5
	+4.2	12.48 ± 0.03	3.7	+5.2	13.26 ± 0.07	2.4	6.1 ± 1.1
	+14.6	12.20 ± 0.02	4.3	+14.6	13.88 ± 0.07	2.4	47.9 ± 8.6
HD 335153	+22.1	11.44 ± 0.02	5.5	...	<9.8	...	<0.02
	-22.9	10.77 ± 0.05	3.3	...	<10.1	...	<0.24
	+5.3	12.15 ± 0.02	5.3	+5.7	12.81 ± 0.05	3.4	4.55 ± 0.63
	+17.9	11.27 ± 0.02	5.4	...	<10.1	...	<0.07
BD+31 4224	+25.4	12.08 ± 0.02	3.9	+25.9	11.90 ± 0.02	2.6	0.67 ± 0.04
	+0.4	11.42 ± 0.02	5.5	+1.5	11.84 ± 0.02	2.3	2.62 ± 0.17
	+7.5	11.62 ± 0.01	4.1	+8.8	11.55 ± 0.01	2.8	0.85 ± 0.03
	+16.3	11.94 ± 0.01	5.0	+16.7	12.32 ± 0.05	1.6	2.42 ± 0.29
HD 198301	+27.9	11.58 ± 0.01	3.7	+29.2	11.64 ± 0.01	2.9	1.15 ± 0.05
	+0.2	11.10 ± 0.02	3.0	+1.0	12.07 ± 0.03	2.3	9.31 ± 0.85
	+7.1	11.55 ± 0.01	3.5	+7.1	12.11 ± 0.05	1.2	3.68 ± 0.43
	+13.3	11.36 ± 0.02	4.6	+11.9	12.04 ± 0.02	3.4	4.78 ± 0.33
BD+31 4256	+20.8	11.29 ± 0.02	3.4	+22.7	11.49 ± 0.01	2.4	1.61 ± 0.08
	+62.2	11.69 ± 0.01	6.4	...	<10.0	...	<0.02
	+82.1	11.60 ± 0.01	6.5	...	<10.0	...	<0.02
	+96.3	11.30 ± 0.02	5.1	...	<10.0	...	<0.05
BD+31 4256	+0.5	11.65 ± 0.02	5.5	+1.1	11.74 ± 0.01	3.3	1.22 ± 0.06
	+9.5	11.87 ± 0.02	4.6	+9.2	11.57 ± 0.01	4.2	0.51 ± 0.02
	+18.4	11.79 ± 0.02	4.5	+19.5	11.29 ± 0.01	2.8	0.31 ± 0.01
HD 335334	-0.5	11.59 ± 0.02	2.8	+1.0	12.39 ± 0.04	2.3	6.26 ± 0.72
	+10.5	11.85 ± 0.01	4.9	+10.5	11.85 ± 0.02	2.4	1.02 ± 0.06
	+21.1	11.23 ± 0.04	5.5	...	<10.0	...	<0.06

Table 4. Column densities (in cm^{-2}) in individual velocity components for the atomic and molecular species observed toward BD+31 4218. The velocities listed are the mean LSR velocities (in km s^{-1}) averaged over all of the species in which a given component is detected. The CN column density refers to the total column density of CN in the $N = 0$ and $N = 1$ levels.

$\langle v_{\text{LSR}} \rangle$	$\log N(\text{Ca II})$	$\log N(\text{Na I})$	$\log N(\text{K I})$	$\log N(\text{Ca I})$	$\log N(\text{CH}^+)$	$\log N(\text{CH})$	$\log N(\text{CN})$
-18.7	10.81 ± 0.04
-2.2	11.78 ± 0.01	12.98 ± 0.06	11.08 ± 0.02	...	12.07 ± 0.16	12.17 ± 0.11	...
+4.1	12.48 ± 0.03	13.26 ± 0.07	11.35 ± 0.02	10.32 ± 0.05	12.69 ± 0.05	12.54 ± 0.05	...
+13.2	12.20 ± 0.02	13.88 ± 0.07	11.97 ± 0.04	10.05 ± 0.06	...	13.33 ± 0.01	12.83 ± 0.02
+22.1	11.44 ± 0.02

SNR (e.g., [Cha & Sembach 2000](#); [Rao et al. 2016, 2017, 2020](#)) and toward one star in the Monoceros Loop ([Dirks & Meyer 2016](#)). If the high-velocity features toward HD 198301 were not present in the spectrum that [Welsh et al. \(2002\)](#) obtained in 2001, then this would represent the first detection of temporal changes in interstellar absorption lines associated with the Cygnus Loop.

Finally, we note the similarity between the sight lines to the [Welsh et al. \(2002\)](#) target HD 197702 and our target BD+31 4218. Both stars are positioned beyond the northwestern boundary of the Cygnus Loop at distances in excess of 1000 pc. Like BD+31 4218, the interstellar Na I column density toward HD 197702 is more than an order of magnitude larger than toward any of the stars at distances less than 1000 pc. [Welsh et al. \(2002\)](#) reported a total Na I column density of $\log N(\text{Na I}) = 14.36 \pm 0.22$ toward HD 197702, while we find $\log N(\text{Na I}) = 14.02 \pm 0.07$ toward BD+31 4218. Both stars are evidently probing different portions of the western molecular cloud that [Fesen et al. \(2018b\)](#) suggested is physically interacting with the Cygnus Loop. Since the Na I column density toward

BD+31 4224, a star positioned just 11'6 away from BD+31 4218, is $\log N(\text{Na I}) = 12.55 \pm 0.04$, the large jump in column density signifying the onset of this molecular cloud must occur at a distance between ~ 730 pc and ~ 1100 pc.

Tighter constraints on the distance to the western molecular cloud can be obtained by considering the 3D dust reddening map provided by [Green et al. \(2019\)](#). [Fesen et al. \(2018a,b\)](#) have already performed a fairly extensive analysis of the variations in reddening with distance that are seen for clouds in the direction of the Cygnus Loop. Their analysis is based on the work of [Green et al. \(2015\)](#), whereas we have used the updated dust map provided by [Green et al. \(2019\)](#). The [Green et al. \(2019\)](#) data² indicate that there is a large jump in $E(B-V)$ in the direction of BD+31 4218, from ~ 0.06 to ~ 0.3 , for distances between 750 pc and 790 pc. A similar jump in reddening is indicated toward HD 197702. In that direction, $E(B-V)$ increases

² Available from: <http://argonaut.skymaps.info/>

abruptly from ~ 0.06 to ~ 0.4 for distances between 790 pc and 840 pc. These limits are consistent with our less stringent constraints based on Na I absorption. In the next section, we discuss the implications of our results for distance estimates to the Cygnus Loop SNR.

4 DISCUSSION

Fesen et al. (2021) recently reported a distance to the Cygnus Loop SNR of 725 ± 15 pc. This result, and its very small uncertainty, was based on the Gaia EDR3 distances to several stars that Fesen et al. (2018a,b) suggested are either interacting directly with the SNR or are positioned behind the expanding shock front. The star that Fesen et al. (2018a) claimed is directly interacting with the Cygnus Loop, due to the appearance of a bow-shock nebula surrounding the star and the chaotic nature of the SNR shocks in the vicinity of the star, is BD+31 4224, which has a Gaia EDR3 distance of 726_{-11}^{+13} pc. While there is qualitative support for the idea that the stellar wind from BD+31 4224 is interacting with the Cygnus Loop’s expanding shocks (see the discussion in Fesen et al. 2018a), the evidence is not conclusive. Another star considered by Fesen et al. (2021) in deriving their distance estimate is KPD 2055+3111, a subdwarf OB star that Blair et al. (2009) reported shows high-velocity O VI absorption (at an LSR velocity of -75 km s^{-1}). KPD 2055+3111 is positioned among the bright optical filamentary structures associated with the Eastern Veil Nebula. Blair et al. (2009) based their analysis of this star on observations taken with the Far Ultraviolet Spectroscopic Explorer (FUSE). The FUSE spectrum of KPD 2055+3111 is rather complicated (see Figure 7 in Blair et al. 2009). However, if the detected O VI absorption is indeed associated with the SNR, then this implies that the distance to the Cygnus Loop is less than that to the star, which has a Gaia EDR3 distance of 819_{-18}^{+21} pc. (More precisely, since the high-velocity O VI absorption is blueshifted, this proves only that the background star is behind the approaching side of the SNR shock front.)

The three other stars that Fesen et al. (2021) considered in deriving their precision distance estimate to the Cygnus Loop are those that Fesen et al. (2018b) claimed show high-velocity Na I and Ca II absorption. The most prominent among these (because it appears to show the clearest example of redshifted and blueshifted Na I and Ca II absorption) is HD 335334 (referred to in Fesen et al. (2018b, 2021) as Star X). However, as we have shown conclusively in this paper, HD 335334 is a double-line spectroscopic binary and shows no evidence for high-velocity interstellar absorption. As such, the distance to this star cannot be used to constrain the distance to the Cygnus Loop. The other two stars are TYC 2688-365-1 (Star Y), and TYC 2692-3378-1 (Star Z). We did not observe these stars with the 2.7 m telescope (because they are somewhat too faint for high-resolution, high S/N ratio spectroscopy). However, from the spectra of these stars presented in Fesen et al. (2018b), the “high-velocity” Na I features appear instead to be broad, stellar Na I absorption lines onto which the narrow low-velocity interstellar Na I components are superimposed. (The Ca II feature in the spectrum of Star Z is clearly a stellar absorption line; see Figure 3 in Fesen et al. 2018b).

One implication of these results involves the detailed morphological orientation of the Cygnus Loop along the line of sight. Fesen et al. (2018b) struggled to obtain a distance estimate that simultaneously met the criteria that BD+31 4224 be inside the remnant and the seemingly closer stars X and Y be behind the remnant. Fesen et al. (2018b) proposed a solution in which the Cygnus Loop’s main northern shell is aspherical and tilted so that these different criteria could be accommodated (see Figures 4 and 5 in Fesen et al. 2018b). Since

neither Star X nor Star Y show evidence of high-velocity interstellar absorption, there is no longer any need for this complicated “solution.” Fesen et al. (2021) pointed to an additional tension that arises with their restrictive distance estimate of only 725 pc. Proper motion measurements of several of the Cygnus Loop’s northern nonradiative Balmer-dominated filaments by Salvesen et al. (2009), combined with a distance of 725 pc, yield shock velocities that are too low compared to the shock velocities determined from line-width measurements of the broad H α emission components at the same filamentary positions (Medina et al. 2014). From their H α emission measurements, Medina et al. (2014) suggested that a more likely distance to the Cygnus Loop SNR is ~ 890 pc. (A reanalysis by Raymond et al. (2015), which considered the effects of thermal equilibration in a collisionless shock, reduced this distance estimate to ~ 800 pc.)

Our discovery of high-velocity Ca II absorption (at LSR velocities of +62, +82, and +96 km s^{-1}) toward HD 198301 implies that the distance to the Cygnus Loop SNR must be less than the distance to this star, which has a Gaia EDR3 distance of 872_{-20}^{+21} pc. Note that the fact that the high-velocity gas is redshifted means that the star must be behind the receding edge of the SNR shock front. The star HD 198301 is positioned in the midst of a bright triangular-shaped filamentary region known as Pickering’s Triangle³ (see Figure 1). The bright optical emission from this region (along with the similarly bright filamentary emission from the Eastern and Western Veil Nebulae) has been interpreted as arising from the interaction of the SNR blast wave with density inhomogeneities in the surrounding interstellar clouds (Levenson et al. 1998; Fesen et al. 2018b). Since the high-velocity shocked gas toward HD 198301 is redshifted, this strongly implies that the density inhomogeneity giving rise to the optical emission associated with Pickering’s Triangle lies on the rear side of the expanding SNR shock front. (A similar argument implies that the shocked gas associated with the Eastern Veil Nebula lies on the near side of the SNR, since the high-velocity O VI absorption toward KPD 2055+3111 is blueshifted.)

Another implication of our results is that the magnitude of the velocities of shocks driven into interstellar clouds by the Cygnus Loop’s blast wave is less than that implied by the analysis of Fesen et al. (2018b). Those authors reported Na I components with velocities ranging from -160 to $+240 \text{ km s}^{-1}$ (toward Star Z). However, as discussed above, these supposed high-velocity “components” are more likely just the extreme portions of the wings of broad stellar Na I absorption lines. The maximum Ca II absorption velocity toward HD 198301 ($+96 \text{ km s}^{-1}$) implies a cloud shock velocity of $\sim 100 \text{ km s}^{-1}$, much less than the 240 km s^{-1} reported by Fesen et al. (2018b). The velocity of the cloud shock toward HD 198301 could be somewhat higher than 100 km s^{-1} if there is a significant tangential component to the motion. Nevertheless, our determination of the (radial component of the) cloud shock velocity toward HD 198301 is consistent with the shock velocities derived from proper motion and emission-line studies of the bright radiative filaments associated with the Cygnus Loop, which indicate shock velocities in the range 100 to 150 km s^{-1} (e.g., Raymond et al. 2020).

High-velocity interstellar absorption features are relatively rare, even among sight lines passing through the optical boundaries of SNRs. From a large survey of Na I and Ca II lines toward stars in the Vela SNR, Cha & Sembach (2000) found that only $\sim 25\%$

³ “Pickering’s Triangle” was discovered photographically in 1904 by Williamina Fleming, an astronomer working at the Harvard College Observatory under the direction of Edward Charles Pickering (see Pickering & Fleming 1906).

of the stars showed high-velocity Ca II components, and only $\sim 12\%$ showed high-velocity Na I. Of the 14 stars in the Cygnus Loop region included in [Welsh et al. \(2002\)](#) and in this paper, only one exhibits high-velocity Ca II absorption. Partly, this is due to a distance effect since many of the [Welsh et al. \(2002\)](#) targets are likely positioned in front of the SNR. However, our targets were deliberately chosen because they are more likely to be background stars, yet only one of our six targets shows high-velocity interstellar absorption. In this context, it is important to remember that low-ionization species, such as Na I and Ca II, do not probe the SNR shock itself. Rather, they probe pre-existing interstellar gas that has been shocked and accelerated by the SNR blast wave. Thus, the detection of high-velocity interstellar Na I or Ca II absorption requires the chance alignment of a shocked interstellar cloud and a bright background star. Such chance alignments are evidently somewhat rare given the highly inhomogeneous nature of the interstellar medium.

5 SUMMARY AND CONCLUSIONS

Six stars were observed at moderately high spectral resolution with the Tull spectrograph and 2.7 m telescope at McDonald Observatory. Low velocity interstellar Na I and Ca II absorption lines are detected in each direction. High-velocity Ca II absorption (at LSR velocities of +62, +82, and +96 km s⁻¹) is detected toward only one star: HD 198301, which lies behind the bright region of filamentary emission known as Pickering’s Triangle. This is the first conclusive detection of high-velocity gas in a low ionization species such as Ca II associated with the Cygnus Loop SNR. This detection means that the receding edge of the Cygnus Loop’s shock front must be in front of HD 198301 (which is at a distance of ~ 870 pc). A previous detection of high-velocity O VI absorption toward KPD 2055+3111 (at -75 km s⁻¹) by [Blair et al. \(2009\)](#) indicates that the approaching side of the shock front must be at a distance of less than ~ 820 pc. While [Fesen et al. \(2021\)](#) constrained the distance to the Cygnus Loop to be 725 ± 15 pc, this result is largely dependent on whether or not the star BD+31 4224 is physically interacting with the Cygnus Loop. However, the evidence suggesting an interaction between this star’s stellar wind and the Cygnus Loop’s expanding shock wave is merely suggestive and not conclusive.

The star HD 335334, which was previously thought to exhibit high-velocity Na I and Ca II absorption ([Fesen et al. 2018b](#)), is actually a double-line spectroscopic binary star. We find no evidence for high-velocity interstellar absorption in this direction, meaning that the distance to HD 335334 cannot be used to constrain the distance to the Cygnus Loop. Two other stars observed by [Fesen et al. \(2018b\)](#) probably also do not exhibit high-velocity interstellar absorption. The “high-velocity” Na I components in these directions are instead portions of the broad stellar Na I absorption lines. The end result of our analysis is that the distance to the Cygnus Loop SNR is not as precisely known as [Fesen et al. \(2021\)](#) have claimed.

Strong interstellar absorption from various atomic and molecular species is detected toward the most distant star in our sample: BD+31 4218, which is positioned to the northwest beyond the bright optical boundary of the Cygnus Loop SNR. This star probes part of an adjacent molecular cloud to the west of the Cygnus Loop. The rear portion of the expanding SNR shock wave appears to be directly interacting with this molecular material, giving rise to the Western Veil Nebula and probably also Pickering’s Triangle. The rise in column density associated with this molecular material is constrained to lie between ~ 730 and ~ 1100 pc. A corresponding jump in $E(B-V)$ in the direction of BD+31 4218 is indicated for distances between 750

and 790 pc ([Green et al. 2019](#)). If the Cygnus Loop SNR is indeed interacting with the background molecular cloud to its west, then the distance to the SNR would likely need to fall within this range. We note that the original [Minkowski \(1958\)](#) value of 770 pc would fit within this constraint.

The physical conditions in the high-velocity shocked material toward HD 198301 could be studied in much greater detail using high-resolution HST/STIS observations in the UV. The UV portion of the spectrum provides access to numerous diagnostic lines that can be used to examine the densities, temperatures, pressures, depletions, and ionization states of shocked interstellar gas (e.g., [Ritchey et al. 2020](#)). However, because HD 198301 is a narrow-lined star, its UV spectrum will be challenging to interpret. Nevertheless, this star provides us with the best (and, indeed, only) opportunity to examine the detailed physical conditions in high-velocity shocked gas associated with the Cygnus Loop SNR using the technique of high-resolution UV absorption-line spectroscopy.

ACKNOWLEDGEMENTS

We thank Coyne Gibson of McDonald Observatory for his help in manually aligning the Tull spectrograph in its TS23 configuration. This research has made use of the SIMBAD database, operated at CDS, Strasbourg, France.

DATA AVAILABILITY

The McDonald Observatory data on which our analysis is based may be available upon request to the corresponding lead author.

REFERENCES

- Bailer-Jones, C. A. L., Rybizki, J., Fouesneau, M., Demleitner, M., & Andrae, R. 2021, *AJ*, 161, 147
- Blair, W. P., Sankrit, R., Raymond, J. C., & Long, K. S. 1999, *AJ*, 118, 942
- Blair, W. P., Sankrit, R., Torres, S. I., Chayer, P., & Danforth, C. W. 2009, *ApJ*, 692, 335
- Blair, W. P., Sankrit, R., & Tulin, S. 2002, *ApJS*, 140, 367
- Cha, A. N., & Sembach, K. R. 2000, *ApJS*, 126, 399
- Danforth, C. W., Blair, W. P., & Raymond, J. C. 2001, *AJ*, 122, 938
- Danks, A. C., & Sembach, K. R. 1995, *AJ*, 109, 2627
- Dirks, C., & Meyer, D. M. 2016, *ApJ*, 819, 45
- Fesen, R. A., Blair, W. P., & Kirshner, R. P. 1982, *ApJ*, 262, 171
- Fesen, R. A., Neustadt, J. M. M., Black, C. S., & Milisavljevic, D. 2018a, *MNRAS*, 475, 3996
- Fesen, R. A., Weil, K. E., Cisneros, I. A., Blair, W. P., & Raymond, J. C. 2018b, *MNRAS*, 481, 1786
- Fesen, R. A., Weil, K. E., Cisneros, I., Blair, W. P., & Raymond, J. C. 2021, *MNRAS*, 507, 244
- Gray, R. O., & Corbally, C. J. 2009, *Stellar Spectral Classification by Richard O. Gray and Christopher J. Corbally*, Princeton Univ. Press, Princeton, NJ
- Gray, R. O., & Corbally, C. J. 2014, *AJ*, 147, 80
- Green, G. M., Schlafly, E. F., Finkbeiner, D. P., et al. 2015, *ApJ*, 810, 25
- Green, G. M., Schlafly, E., Zucker, C., Speagle, J. S., & Finkbeiner, D. 2019, *ApJ*, 887, 93
- Levenson, N. A., Graham, J. R., Keller, L. D., & Richter, M. J. 1998, *ApJS*, 118, 541
- Medina, A. A., Raymond, J. C., Edgar, R. J., et al. 2014, *ApJ*, 791, 30
- Minkowski, R. 1958, *Rev. Mod. Phys.*, 30, 1048
- Mooley, K., Hillenbrand, L., Rebull, L., Padgett, D., & Knapp, G. 2013, *ApJ*, 771, 110

Munari, U., Sordo, R., Castelli, F., & Zwitter, T. 2005, *A&A*, 442, 1127

Pan, K., Federman, S. R., Sheffer, Y., & Andersson, B.-G. 2005, *ApJ*, 633, 986

Patnaude, D. J., Fesen, R. A., Raymond, J. C., et al. 2002, *AJ*, 124, 2118

Pickering, E. C., & Fleming, W. P. 1906, *ApJ*, 23, 257

Rao, N. K., Lambert, D. L., Reddy, A. B. S., et al. 2017, *MNRAS*, 467, 1186

Rao, N. K., Lambert, D. L., Reddy, A. B. S., et al. 2020, *MNRAS*, 493, 497

Rao, N. K., Muneer, S., Lambert, D. L., & Varghese, B. A. 2016, *MNRAS*, 455, 2529

Raymond, J. C., Black, J. H., Dupree, A. K., Hartmann, L., & Wolff, R. S. 1981, *ApJ*, 246, 100

Raymond, J. C., Chilingarian, I. V., Blair, W. P., et al. 2020, *ApJ*, 894, 108

Raymond, J. C., Edgar, R. J., Ghavamian, P., & Blair, W. P. 2015, *ApJ*, 805, 152

Raymond, J. C., Ghavamian, P., Williams, B. J., et al. 2013, *ApJ*, 778, 161

Raymond, J. C., Seok, J. Y., Koo, B.-C., et al. 2023, *ApJ*, 954, 34

Ritchey, A. M. 2020, *MNRAS*, 495, 2909

Ritchey, A. M., Jenkins, E. B., Federman, S. R., et al. 2020, *ApJ*, 897, 83

Ritchey, A. M., Federman, S. R., & Lambert, D. L. 2011, *ApJ*, 728, 36

Sallmen, S., & Welsh, B. Y. 2004, *A&A*, 426, 555

Salvesen, G., Raymond, J. C., & Edgar, R. J. 2009, *ApJ*, 702, 327

Sankrit, R., Blair, W. P., Raymond, J. C., & Long, K. S. 2000, *AJ*, 120, 1925

Sankrit, R., Williams, B. J., Borkowski, K. J., et al. 2010, *ApJ*, 712, 1092

Schmidt-Kaler, T. 1982, in *Landolt-Bornstein Numerical Data and Functional Relationships in Science and Technology, Group VI, Vol. 2b*, Springer-Verlag, Berlin

Sheffer, Y., Rogers, M., Federman, S. R., et al. 2008, *ApJ*, 687, 1075

Tull, R. G., MacQueen, P. J., Sneden, C., & Lambert, D. L. 1995, *PASP*, 107, 251

Wegner, W. 1994, *MNRAS*, 270, 229

Welsh, B. Y., Sallmen, S., Sfeir, D., & Lallement, R. 2002, *A&A*, 391, 705

Welty, D. E., Federman, S. R., Gredel, R., Thorburn, J. A., & Lambert, D. L. 2006, *ApJS*, 165, 138

Welty, D. E., & Hobbs, L. M. 2001, *ApJS*, 133, 345

Welty, D. E., Hobbs, L. M., & Kulkarni, V. P. 1994, *ApJ*, 436, 152

Welty, D. E., Morton, D. C., & Hobbs, L. M. 1996, *ApJS*, 106, 533

Wenger, M., Ochsenbein, F., Egret, D., et al. 2000, *A&AS*, 143, 9

APPENDIX A: STELLAR SPECTRAL CLASSIFICATION

Before this investigation, most of our targets had very little reliable information available regarding their spectral types and luminosity classes. This was especially problematic for HD 198301 and HD 335334. Both stars exhibit narrow stellar absorption lines, making the task of distinguishing between stellar absorption and interstellar absorption challenging. For this reason, and because our spectra cover nearly the entire optical range, we sought to obtain more accurate information regarding the spectral classification of our stars.

The first step toward classifying our targets was to create classification grade spectra from our high-resolution echelle data. By “classification grade” we mean low-resolution, continuum-normalized spectra in the blue-violet region ($\sim 3800\text{--}4600\text{ \AA}$). The individual echelle orders from our high-resolution data were carefully normalized and merged into a continuous spectrum. Then, using computer programs associated with the spectral classification routine MKCLASS⁴ (Gray & Corbally 2014), the normalized spectra were smoothed to a resolution of 1.8 \AA and rebinned to a spacing of 1 \AA . The resulting classification grade spectra are shown in Figure A1.

Initial spectral types were determined by comparing the heavily smoothed spectra of our targets with the library of standard spectra provided with the MKCLASS program. More quantitative results

Table A1. Best-fitting model parameters for the program stars (excluding the Be star BD+31 4218) determined by comparing the observed spectra to the high-resolution synthetic spectra of Munari et al. (2005). We list model parameters for both components of the spectroscopic binary star HD 335334.

Star	T_{eff} (K)	$\log g$	$v \sin i$ (km s^{-1})
HD 335153	11,000	3.5	250
BD+31 4224	13,000	4.0	200
HD 198301	12,000	3.5	20
BD+31 4256	11,000	3.5	200
HD 335334A	10,500	3.5	20
HD 335334B	10,500	4.0	20

were then obtained by measuring the equivalent widths of prominent absorption lines in our program stars and comparing our measurements to similar measurements made for spectral-type standards (Mooley et al. 2013). In particular, we measured equivalent widths for Ca II $\lambda 3933$, He I $\lambda 4009$, He I $\lambda 4026$, H δ $\lambda 4101$, He I $\lambda 4143$, H γ $\lambda 4340$, He I $\lambda 4471$, Mg II $\lambda 4481$, H β $\lambda 4862$, and He I $\lambda 4921$. Since the He I lines weaken, while lines such as Ca II $\lambda 3933$ and Mg II $\lambda 4481$ strengthen, with decreasing temperature for late B into early A stars (Gray & Corbally 2009), the He I $\lambda 4471$ /Mg II $\lambda 4481$ equivalent width ratio was especially useful for deriving temperature types for our stars. Luminosity classes were then obtained by comparing the detailed shapes of the H Balmer lines to those of the standard stars from the MKCLASS library.

The final derived spectral types and luminosity classes for our targets are provided in Table 1. One of our targets, BD+31 4218, is a Be star, with prominent double-peaked emission in many of the H Balmer lines, including H α , H β , H γ , and H δ . It was more difficult to derive a luminosity class for this star since the shapes (and absorption strengths) of the Balmer lines are modified by emission. However, we found that the spectrum of BD+31 4218 closely resembled that of the B2 IVpne star HD 88661 (see Figure 4.17 in Gray & Corbally 2009), although our target exhibits somewhat less emission in the Balmer lines than does HD 88661. Our equivalent width analysis had already yielded a spectral type of B2 for BD+31 4218. We therefore adopted the luminosity class from HD 88661 for BD+31 4218.

We checked the accuracy of our derived spectral types by comparing the unsmoothed (high-resolution) spectra of our targets to the library of high-resolution stellar model spectra provided by Munari et al. (2005). The Munari et al. (2005) library provides a maximum resolving power of $R = 20,000$, which is not quite as high as the resolving power achieved with our spectra ($R \approx 66,000$). Nevertheless, comparison with the Munari et al. (2005) models proved useful, especially for the two stars in our sample with narrow absorption lines (see Section 3.1). The grid of Munari et al. (2005) models for late B stars has steps in T_{eff} of 500 K or 1,000 K and steps in $\log g$ of 0.5 dex. We considered solar metallicity models only. For a given star, we compared the observed high-resolution spectrum to a grid of models with T_{eff} and $\log g$ close to that of the derived spectral type and luminosity class. We also tested several different values of the projected rotational velocity. The derived best-fitting values of T_{eff} , $\log g$, and $v \sin i$ are provided in Table A1. We list model parameters for both components of the spectroscopic binary star HD 335334. These are the parameters that were used to construct the composite spectra discussed in Section 3.1.2. The star BD+31 4218 is not included in Table A1 because it would not be appropriate to compare the observed spectrum of this Be star with the model spectra provided by Munari et al. (2005). In general, the best-fitting model parameters

⁴ Available from: <http://www.appstate.edu/~grayro/mkclass/>

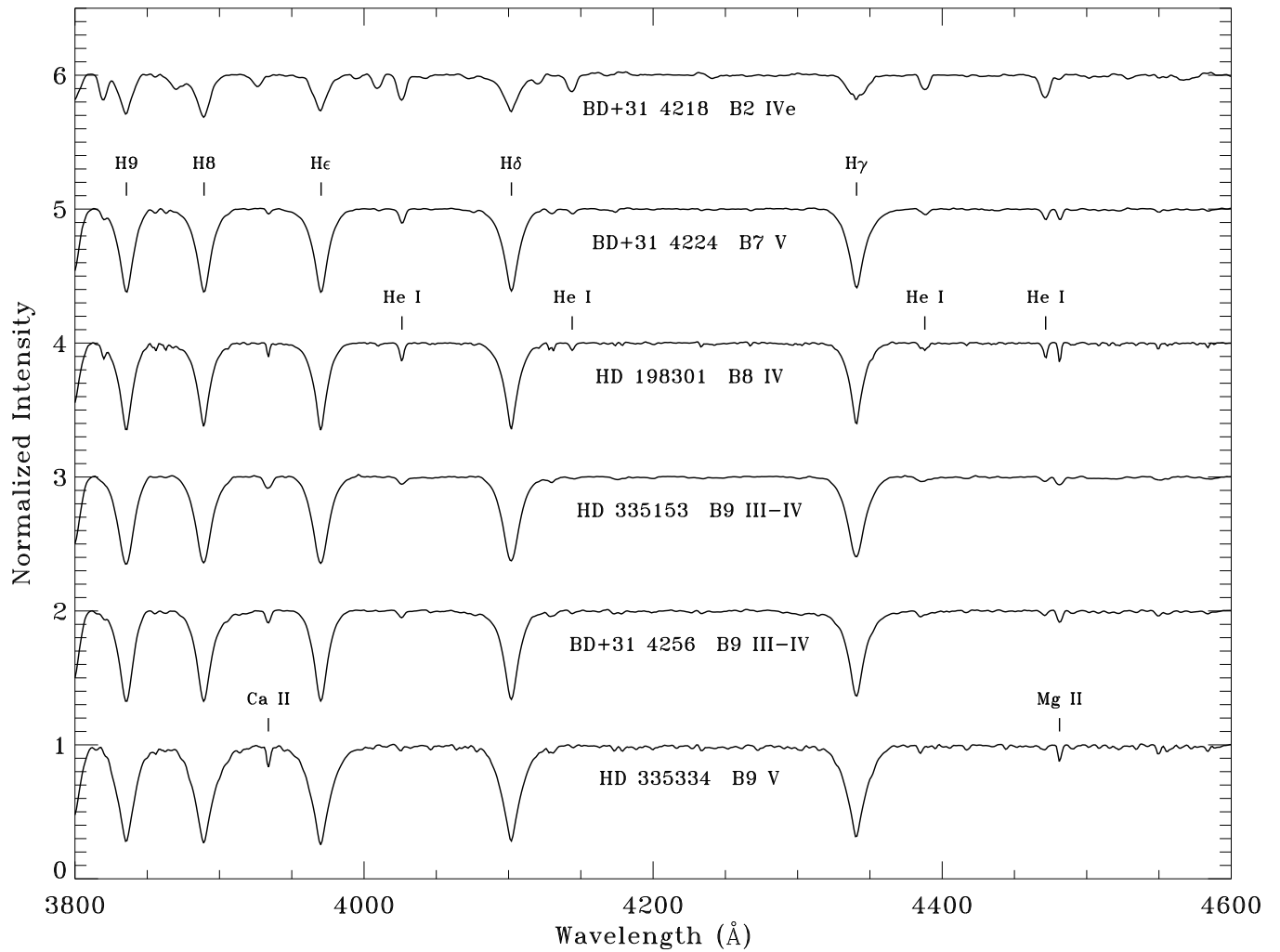


Figure A1. Heavily smoothed spectra of the program stars used for stellar classification. The observed spectra have been normalized to the continuum, smoothed to a resolution of 1.8 \AA , and rebinned to a spacing of 1 \AA . The spectra are offset from one another for clarity. Prominent stellar absorption features used in the classification process are labelled.

listed in Table A1 help to confirm the spectral types and luminosity classes previously derived for our program stars.

This paper has been typeset from a $\text{T}_{\text{E}}\text{X}/\text{L}^{\text{A}}\text{T}_{\text{E}}\text{X}$ file prepared by the author.